Full Length Article

MnS/MnO heterostructures with dual ion defects for high-performance aqueous magnesium ion capacitors

Minghui Liu[a], Mudi Li[a], Siwen Zhang[a,*], Yaxi Ding[a], Ying Sun[a], Jiazhuo Li[a], Haixi Gu[a], Bosi Yin[a,*], Hui Li[b], Tianyi Ma[b,*]

[a] Institute of Clean Energy Chemistry, Key Laboratory for Green Synthesis and Preparative Chemistry of Advanced Material, College of Chemistry, Liaoning University, Shenyang 110036, PR China
[b] School of Science, RMIT University, Melbourne VIC 3000, Australia

Abstract

The advancement of aqueous magnesium ion energy storage devices encounters limitations due to the substantial hydration radius of magnesium ions (Mg^{2+}) and their strong electrostatic interaction with the primary material. Consequently, this study successfully developed a MnS/MnO heterostructure through a straightforward hydrothermal and annealing method, marking its initial application in aqueous magnesium ion capacitors (AMICs). The fabricated MnS/MnO heterostructure, characterized by S defects, also generates Mn defects via in-situ initiation of early electrochemical processes. This unique dual ion defects MnS/MnO heterostructure (DID-MnS/MnO) enables the transformation of MnS and MnO, initially not highly active electrochemically for Mg^{2+}, into cathode materials exhibiting high electrochemical activity and superior performance. Moreover, DID-MnS/MnO enhances conductivity, improves the kinetics of surface redox reactions, and increases the diffusion rate of Mg^{2+}. Furthermore, this study introduces a dual energy storage mechanism for DID-MnS/MnO, which, in conjunction with dual ion defects, offers additional active sites for Mg^{2+} insertion/deinsertion in the host material, mitigating volume expansion and structural degradation during repeated charge-discharge cycles, thereby significantly enhancing cycling reversibility. As anticipated, using a three-electrode system, the developed DID-MnS/MnO demonstrated a discharge specific capacity of 237.9 mAh/g at a current density of 0.1 A/g. Remarkably, the constructed AMIC maintained a capacity retention rate of 94.3 % after 10000 cycles at a current density of 1.0 A/g, with a specific capacitance of 165.7 F/g. Hence, DID-MnS/MnO offers insightful perspectives for designing alternative clean energy sources and is expected to contribute significantly to the advancement of the clean energy sector.

© 2024 Chongqing University. Publishing services provided by Elsevier B.V. on behalf of KeAi Communications Co. Ltd.
This is an open access article under the CC BY-NC-ND license (http://creativecommons.org/licenses/by-nc-nd/4.0/)
Peer review under responsibility of Chongqing University

Keywords: DID-MnS/MnO; Dual ion defects; Initial electrochemical process-induced defects; Dual energy storage mechanism; Aqueous magnesium ion capacitors.

1. Introduction

In recent times, lithium batteries have prevailed in the energy market; however, with the ongoing shift towards social development, there is a pressing need to explore new clean and renewable energy sources [1–4]. Owing to the ample availability of magnesium, its affordability, high safety, and environmental benefits, aqueous magnesium ion energy storage devices have garnered significant interest from researchers within the industry in recent years [5–9]. The ion radius of Mg^{2+} matches that of lithium ions (Li^+), but its capacity to transfer charge is double that of the monovalent Li^+, which could enhance their electrochemical performance. Nevertheless, this advantage is offset by the strong electrostatic interaction between the divalent Mg^{2+} and electrode materials, coupled with the slow diffusion kinetics and pronounced polarization of Mg^{2+}, which have emerged as major obstacles to their development. Furthermore, a critical challenge

remains in the poor cyclic reversibility due to the main material's structure collapsing after Mg^{2+} insertion. Thus, identifying suitable electrode materials that can address the rate performance and long cycle performance challenges in aqueous magnesium ion energy storage devices holds significant importance [10–13].

Most of the existing research on cathode materials for aqueous magnesium-ion energy storage devices has focused on manganese-based materials, mainly manganese-based oxide materials such as MnO_2, Mn_2O_3, and Mn_3O_4, but there is little research on MnO and manganese-based sulfides [12,13]. MnS and MnO are very attractive cathode materials for use in aqueous magnesium-ion energy storage devices. MnS not only has abundant reserves and a low price but also has a high theoretical capacity (616 mAh/g) and a low redox potential. MnO is also regarded as promising due to its low conversion potential, minimal voltage hysteresis (<0.8 V), and high density (5.43 g/cm^3). Nonetheless, MnS and MnO share the common disadvantages of transition metal sulfides/oxides, such as diminished electrochemical cycling stability attributed to significant volume changes during repeated charging and discharging cycles, alongside lower conductivity and ion mobility, resulting in subpar rate capability [14–17]. To mitigate these issues, researchers have employed various strategies. Ma et al. synthesized S-doped carbonaceous mesoporous frameworks (α-MnS/SCMFs) composite structures exhibiting exceptional performance [15]. Yasoda et al. successfully created MnS/GO/PANI nanocomposites, improving the interfacial interactions between materials of differing sizes; thus, enhancing specific capacitance [18]. Wang et al. developed a MnO/C microsphere structure with excellent reversibility within its operating voltage range and outstanding Li^+ storage capacity [19]. Furthermore, Guo et al. produced carbon-coated MnO porous microspheres, which demonstrated exhibited superior cycling and rate performances, primarily due to the carbon coating's effective buffering of volume changes and improved electronic conductivity [20]. However, the synthesis methods for MnS and MnO are often overly complex or costly, significantly impeding their commercial advancement. Consequently, comprehensive research on MnS and MnO is deemed necessary. Additionally, defect engineering is considered a highly effective approach to modulate the electronic structure of materials, with defective sites proven to anchor additional storage/adsorption/active sites for foreign ions or intermediates during reactions. Introducing defects onto material surfaces can significantly modify the intrinsic electronic structure of manganese-based materials, boost their inherent conductivity, and accelerate the kinetics of surface redox reactions [21]. Xiong et al. enhanced a battery's capacity to 345 mAh/g by incorporating oxygen defects into the MnO_2 lattice, reducing the electrons needed for Zn-O bonding and allowing more valence electrons to join the material's delocalized electron cloud [22]. Zhang et al. integrated Mn defects into the spinel structure of $ZnMn_2O_4$, revealing that Mn defects can effectively lower the electrostatic barrier for Zn^{2+} diffusion and improve reaction kinetics [23].

Hence, this study utilizes a conventional one-step hydrothermal method to produce precursors, which are then converted into MnS/MnO heterostructures through calcination of these precursors. The resulting structure, featuring S defects and in-situ electrochemically induced Mn defects during the initial charging phase, ultimately forms the DID-MnS/MnO. This initial charging process significantly improves the originally suboptimal electrochemical performance of MnS and MnO towards Mg^{2+}, transforming them into electrochemically active cathode materials and marking the inaugural application of MnS/MnO heterostructures in aqueous magnesium ion capacitors with notably superior electrochemical performance. It was observed that both MnS and MnO contribute to energy storage in DID-MnS/MnO, facilitating a dual energy storage mechanism that significantly aids Mg^{2+} insertion/deinsertion in the host material, leading to enhanced cyclic reversibility. The developed AMICs not only achieved a specific capacitance of 330.2 F/g at a current density of 0.1 A/g but also reached an energy density of 148.7 Wh/kg. This strategy holds promise for broad application in the new energy storage sector, offering insights into the development of aqueous magnesium ion energy storage devices and potentially other aqueous ion batteries.

2. Results and discussion

To further develop the potential of manganese-based materials in aqueous magnesium ion energy storage devices and optimize the materials through defect engineering to achieve superior electrochemical performance and promote the development of magnesium ion energy storage devices, we conducted a series of experimental explorations and verifications. Fig. 1 illustrates the synthesis process of the original MnS with a polyhedral structure and the MnS/MnO heterostructure with a popcorn structure. Both target products are synthesized through a one-step hydrothermal method followed by annealing to obtain the final products. The sole distinction lies in the altered hydrothermal reaction temperature for the MnS/MnO heterostructure compared to the original MnS.

The crystal structures of MnS and MnS/MnO were analyzed using X-ray diffraction (XRD), as demonstrated in Fig. 2a The XRD patterns exhibited distinct peaks, indicating the high crystallinity of the samples. The diffraction peaks of the MnS samples were observed sequentially at 29.5°, 34.2°, 49.1°, 58.4°, 61.2°, 72.0°, and 79.7°, corresponding to the (111), (200), (220), (311), (222), (400), and (331) crystal planes of cubic MnS, respectively (PDF # 72-1534). In contrast, MnS/MnO exhibited new diffraction peaks at 34.9°, 40.5°, 58.7°, 70.1°, and 73.8°, corresponding to the (111), (200), (220), (311), and (222) crystal planes of cubic MnO, respectively (PDF # 71-1177). The diffraction peaks of the sample match well, and there are no impurity peaks, indicating the successful preparation of MnS/MnO heterostructures. Scanning electron microscopy (SEM) images have revealed the morphology and microstructure of the MnS/MnO heterostructures. According to Fig. S1a-b in the Supplementary Information, the original MnS is characterized by a polyhe-
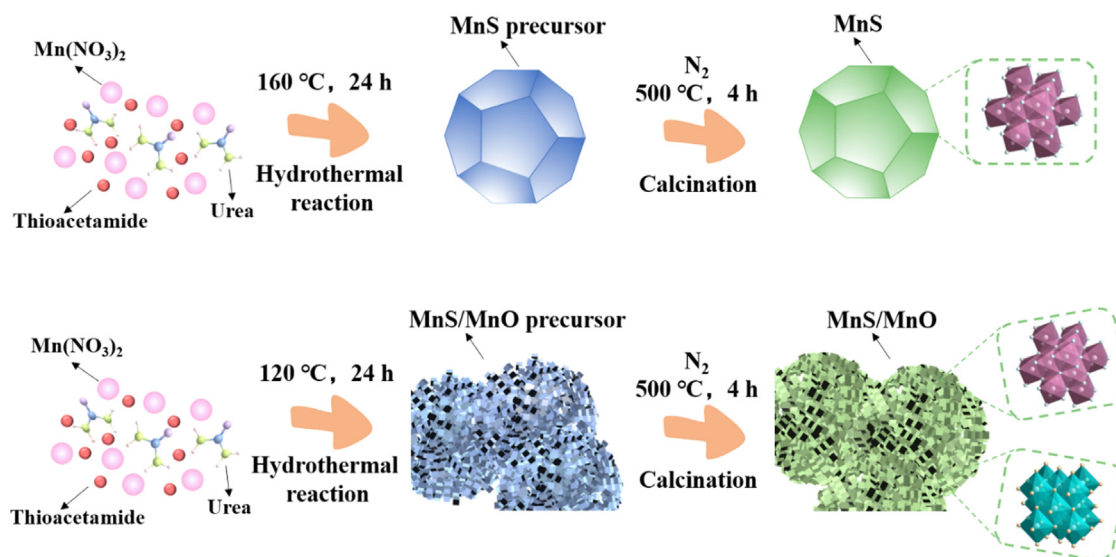
Fig. 1. Preparation process of MnS and MnS/MnO.

dral structure with an approximate size of 10 μm. Furthermore, the elemental distribution within MnS is shown to be uniform, as indicated by the element mapping diagram (Fig. S2a-c, Supplementary Information) and the energy-dispersive X-ray spectroscopy (EDS) results (Fig. S3, Supplementary Information). Notably, the MnS/MnO heterostructure, as depicted in Fig. 2b-c, displays a popcorn structure composed of stacked particles and blocks, with an average size of around 20 μm. The element mapping diagram (Fig. 2d-g) and the EDS spectrum (Fig. S4, Supplementary Information) reveal a uniform distribution of Mn and O elements within the MnS/MnO heterostructure, whereas S elements exhibit noticeable gaps. This observation, along with the Mn to S element ratio not being precisely 1:1 as indicated by the EDS spectrum, indirectly confirms the presence of S defects in the MnS/MnO heterostructure, a topic that will be further explored in later discussions. To delve deeper into the chemical structure of the heterostructure, the Raman spectrum (Fig. S5, Supplementary Information) identified specific peaks at approximately 650 and 580 cm^{-1} in the MnS/MnO samples, which are attributed to the 2TO phonons in the MnS and MnO phases, respectively. These peaks, representing the vibrational bands of Mn-S and Mn-O, confirm the presence of both MnS and MnO phases. This finding aligns with XRD results and underscores the successful synthesis of MnS/MnO heterostructures [24,25]. X-ray photoelectron spectroscopy (XPS) was employed to ascertain the composition and surface elemental states of both the original MnS and the MnS/MnO heterostructures. The XPS analysis (Fig. S6, Supplementary Information) evidenced significant amounts of Mn, S, and O elements in the samples. High-resolution spectra of the MnS/MnO heterostructure and original MnS (Fig. 2h and Fig. S7a, Supplementary Information) each displayed two principal peaks corresponding to Mn $2p_{1/2}$ and Mn $2p_{3/2}$, located at 653.47 eV and 641.65 eV, respectively [26]. The spin-orbit splitting at 11.8 eV pertains to the Mn 2p core energy level, suggesting the presence of Mn^{2+} and aligning with typical reported values for MnS and MnO [27,28]. Furthermore, the peak at 641.65 eV can be deconvoluted into peaks at 641.47 eV and 644.39 eV, corresponding to Mn^{2+} and Mn^{4+}, respectively. The intensity of high-valence manganese is relatively low, possibly because of oxidation of the material surface when in contact with dissolved oxygen during the synthesis process [29]. The high valent manganese's theoretical capacity significantly contributes to enhancing the material's capacity [29]. Additionally, high-resolution energy spectra of S 2p in both the MnS/MnO heterostructures and the original MnS are shown in Fig. 2i and Fig. S7b (Supplementary Information). Peaks at 163.70 eV, 162.22 eV, and 161.04 eV correspond to S-O bonds, S $2p_{1/2}$, and S $2p_{3/2}$, respectively, while a peak at 168.72 eV is indicative of SO_x, a sulfate resulting from sample oxidation [30]. Lastly, the O 1 s high-resolution spectrum of the MnS/MnO heterostructure (Fig. 2j) presents three sub-peaks, with the one at 530.0 eV associated with the typical Mn-O bond in MnO, and the remaining two peaks at 531.67 eV and 532.41 eV related to the -OH and surface-adsorbed oxygen [31–33]. Fig. 2k shows the results of electron paramagnetic resonance (EPR) spectroscopy of the MnS heterostructure. It is not difficult to see that the sample exhibits a highly symmetric signal near the g value of free electrons, which is attributed to the contribution of S defects, further proving the existence of S defects, which means that we synthesized MnS with S defects (SD-MnS) [32]. It is worth noting that the presence of these S defects is expected to provide more active sites for the insertion/deinsertion of magnesium ions (Mg^{2+}) and thus achieve remarkable electrochemical performance [33,34]. Furthermore, we also conducted EPR spectroscopy on the initial and first fully charged electrodes of the MnS/MnO heterostructure. Fig. 2l clearly shows that there are no Mn defects in the initial electrode. However, after in situ induction during a charging process, the first fully charged electrode shows obvious Mn defects
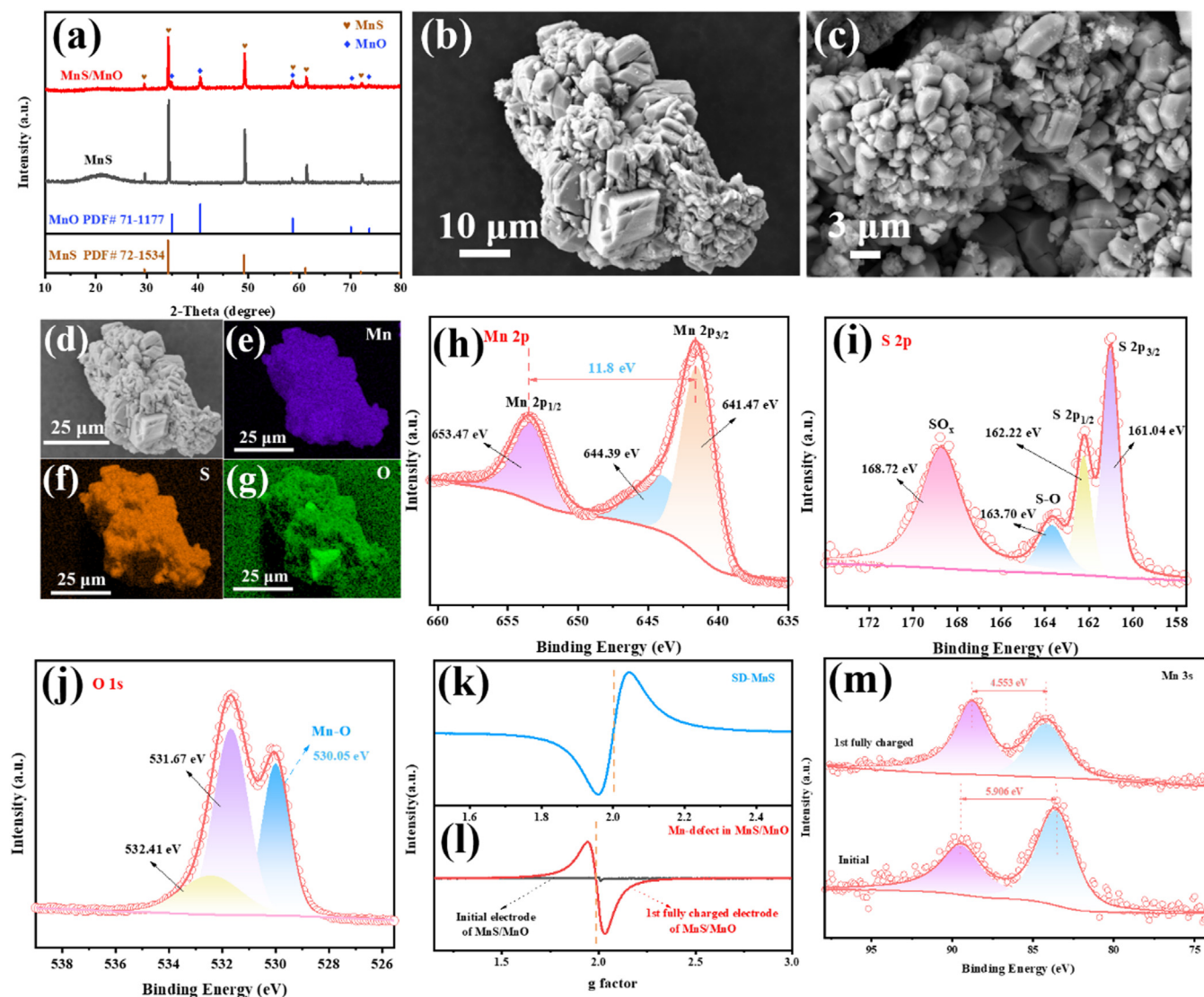
Fig. 2. (a) XRD patterns of the MnS and MnS/MnO heterostructure, (b-c) SEM images of the MnS/MnO heterostructure, (d-g) elemental mapping images of the MnS/MnO heterostructure for (e) Mn, (f) S, and (g) O, (h) Mn 2p, (i) S 2p, and (j) O 1 s for the XPS spectra of the MnS/MnO heterostructure, (k) EPR image of the S-D MnS, (l) EPR image of initial and first full charged electrode of DID- MnS/MnO, (m) Ex-situ XPS spectrum of Mn 3s of initial and first fully charged electrode of DID- MnS/MnO.

[35–37]. As commonly understood, due to the Jahn-Teller effect, most manganese-based active materials inevitably dissolve into the electrolyte during the electrochemical cycling process. The cyclic voltammetry (CV) curve of the MnS/MnO heterostructure, as depicted in Fig. S8 (Supplementary Information), shows a notable phenomenon. Unlike previously reported manganese-based materials, the initial scanning process reveals a distinct oxidation peak at 0.75 V [38]. This peak vanishes in the second scan, and the peak position stabilizes in subsequent scans. The emergence of this peak, resulting from the deintercalation of Mn^{2+} from MnO, reaffirms the existence of Mn defects, which are unveiled during the initial charging process [39]. Thus, the primary source of Mn defects in this study is the dissolution of Mn from the matrix material, and the presence of Mn^{2+} in the electrolyte mitigates further dissolution in subsequent cycles [40]. The ex-situ XPS spectrum of Mn 3 s (Fig. 2m) initially shows a peak energy separation of 5.906 eV, closely matching that of Mn^{2+}. Remarkably, the spectrum indicates a decrease in the peak energy separation of Mn 3 s after initial charging (5.906 → 4.553 eV), suggesting an increase in the oxidation state of Mn due to the deinsertion of Mn^{2+} from the MnO matrix into the electrolyte, further validating the presence of Mn defects. This study has thus established the material as a dual ion defects MnS/MnO heterostructure (DID-MnS/MnO). The existence of Mn defects elevates the average valence state of manganese ions in the material, enhancing the electrochemical activity of MnO for Mg^{2+} and facilitating Mg^{2+} transfer [41]. More crucially, Mn defects create more accessible pathways for ion transport, diminishing the diffusion barrier for Mg^{2+}, and enhancing its insertion/deinsertion in host materials. The synergistic effect of S defects and in-situ induced Mn

defects, a dual ion defect mechanism, leads to improved electrochemical performance of the active material. N_2 adsorption/desorption isotherm tests were conducted to examine the specific surface area and pore structure of the material further. According to the International Union of Pure and Applied Chemistry (IUPAC) classification, the material exhibits typical type IV isotherms with type H3 hysteresis loops, confirming mesoporous structures [42]. The original SD-MnS has a relatively modest specific Brunauer-Emmett-Teller (BET) surface area of only 0.5366 m^2/g. However, for DID-MnS/MnO, this value increases significantly to 4.6145 m^2/g (Fig. S9a, Supplementary Information). The Barrett-Joyner-Helenda (BJH) pore size distribution (Fig. S9b, Supplementary Information) of DID-MnS/MnO shows a substantial improvement in void volume to 0.051805 cm^3/g from the original SD-MnS at 0.003747 cm^3/g. These findings confirm that DID-MnS/MnO possesses a higher specific surface area and pore size distribution, providing more active sites for Mg^{2+} and enhancing the interaction between the electrolyte and the active material. This accelerates the Mg^{2+} insertion/deinsertion rate, thereby improving the capacity and cycling performance of the active material [43,44].

To validate the excellent magnesium storage capacity of DID-MnS/MnO, a series of electrochemical tests were performed using a three-electrode system within a working voltage range of -0.8–1.1 V. The CV curve (Fig. 3a) at a scanning rate of 0.2 mV/s demonstrates that compared to the original SD-MnS, the electrode with DID-MnS/MnO exhibits stronger redox peak currents and a larger peak area. Remarkably, the voltage intervals for DID-MnS/MnO are 0.74 V and 0.55 V, significantly lower than those for SD-MnS (0.99 V and 0.60 V), indicating reduced polarization in DID-MnS/MnO [45]. These observations signify enhanced reactivity and more complete redox reactions in DID-MnS/MnO, contributing to a superior magnesium storage capacity. Furthermore, at a scanning rate of 1.0 mV/s, the CV curve (Fig. 3b) shows an impressive degree of overlap, further indicating the excellent stability of DID-MnS/MnO after the initial scanning process, beneficial for Mg^{2+} insertion/deinsertion and achieving enhanced long-term cycling performance. Under consistent conditions, the galvanostatic charge/discharge (GCD) curves of both the original SD-MnS and DID-MnS/MnO were analyzed at varying current densities of 0.1, 0.2, 0.3, 0.5, 0.8, and 1.0 A/g, as shown in Fig. 3c and Fig. S10 (Supplementary Information). The comparison of GCD curves at a 1.0 A/g current density, depicted in Fig. 3d, demonstrates that DID-MnS/MnO exhibits superior plateau characteristics, maintaining a long and stable discharge plateau even at higher current densities. This evidence confirms its exceptional reversibility and outstanding electrochemical performance. Fig. 3e presents a comparison of the long-term cycle performance and Coulombic efficiency between DID-MnS/MnO and the original SD-MnS at a current density of 1.0 A/g. After 1200 cycles, DID-MnS/MnO maintains a discharge specific capacity of 90.1 mAh/g, with a capacity retention rate of 94.7 %. In contrast, the original SD-MnS rapidly loses electrochemical activity after 700 cycles, and its Coulombic efficiency lacks stabil-

ity. These results indicate that DID-MnS/MnO possesses enhanced structural stability and reversibility, facilitating Mg^{2+} insertion/deinsertion, thereby achieving higher capacity and improved long-term cycling capability. The rate performance comparison, shown in Fig. 3f, illustrates that DID-MnS/MnO achieves discharge specific capacities of 237.9, 161.8, 141.3, 117.8, 101.7, and 95.9 mAh/g, which are significantly superior to those of the original SD-MnS across various current densities. Additionally, the discharge specific capacity of DID-MnS/MnO surpasses that of most reported aqueous magnesium ion energy storage devices, highlighting its substantial potential (Fig. 3g, Table S1, Supplementary Information). Electrochemical impedance spectroscopy (EIS) analysis was conducted to examine the charge transfer kinetics and interface charge transfer resistance of the electrode materials. The equivalent circuit diagram includes solution resistance (R_s), charge transfer resistance (R_{ct}), a capacitive element (CPE1), and Warburg impedance (W_0), corresponding to Mg^{2+} diffusion to the cathode electrode (Fig. 3h). The DID-MnS/MnO electrode material exhibits a significantly lower R_{ct} (4.441 Ω) compared to the SD-MnS electrode (5.399 Ω), indicating faster Mg^{2+} diffusion kinetics and reduced interface charge transfer resistance. This demonstrates that Mn defects and S defects enhance Mg^{2+} diffusion.

Subsequently, to further confirm the electrochemical kinetics of DID-MnS/MnO and SD-MnS, CV tests were conducted at various scan rates ranging from 0.2 to 1.0 mV/s, as illustrated in Fig. 4a and Fig. S11a (Supplementary Information). It is evident that both materials display two oxidation peaks and two reduction peaks, aligning with the charge-discharge curve. The correlation between peak current (*i*) and scanning rate (*v*) can be assessed using the empirical formula [46]:

$$i = av^b \tag{1}$$

This relationship can also be expressed as:

$$\log(i) = b\log(v) + \log(a) \tag{2}$$

where *i* represents the peak current, *v* represents the scan rate, and a and b are variable values associated with the type of capacity contribution. Typically, if the *b* value approaches 0.5, the charging and discharging process are primarily controlled by diffusion. If the *b* value approaches 1, the charging and discharging process are mainly governed by capacitive behavior. In DID-MnS/MnO, the slopes of the log (*i*) and log (*v*) curves for the four redox peaks are depicted in Fig. 4b. The *b* values for peak 1, peak 2, peak 3, and peak 4 are 0.78, 0.91, 0.53, and 0.75, respectively, indicating contributions from both diffusion and capacitance processes. The *b* values of SD-MnS are shown in Fig. S11b (Supplementary Information). The *b* values for peak 1, peak 2, peak 3, and peak 4 are 0.53, 0.66, 0.65, and 0.52, respectively, indicating mainly diffusion process contribution. To further quantify the diffusion contribution and capacitance contribution ratio of Mg^{2+}, the capacitance contribution can be calculated using the following formula [47]:
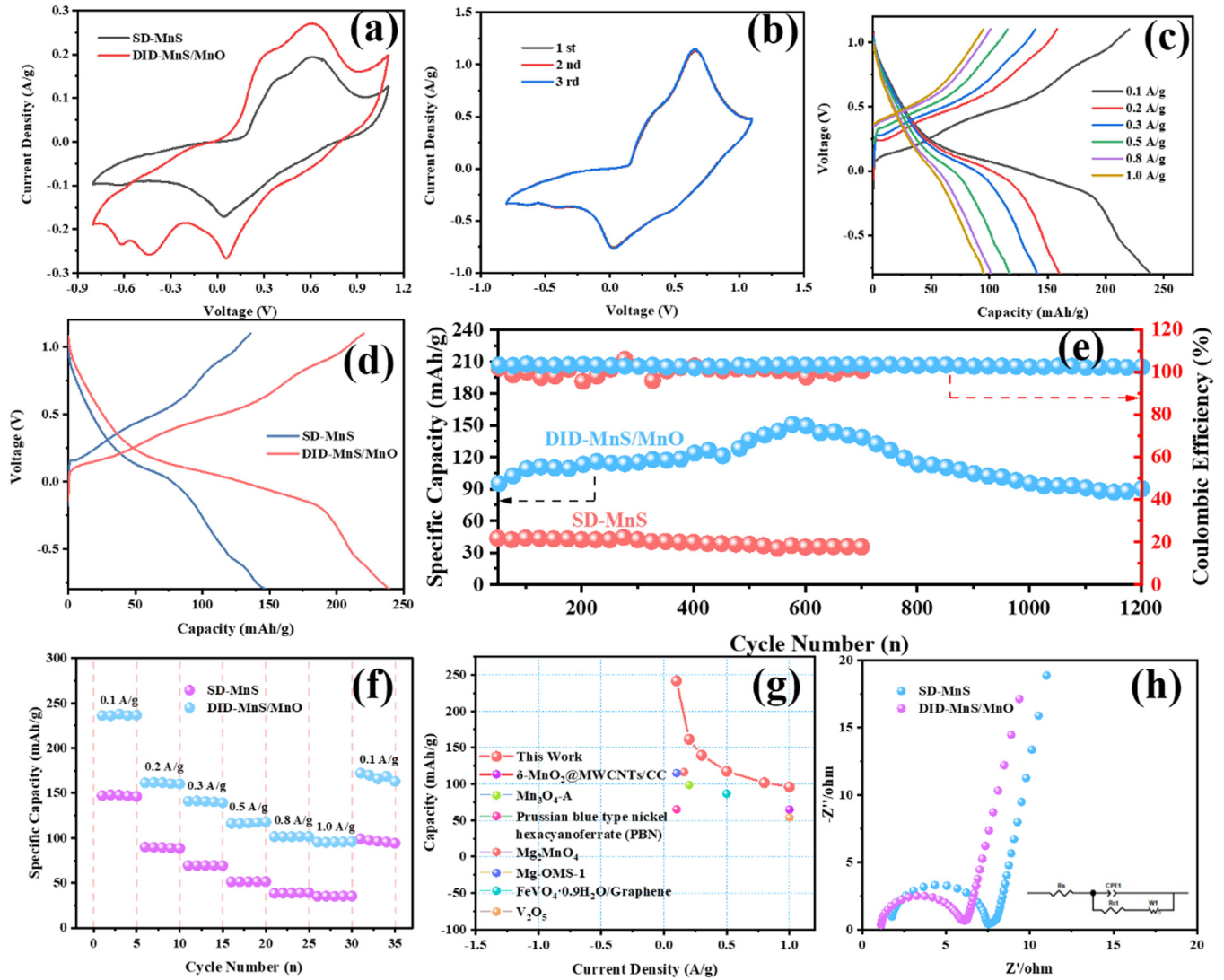
$$i = k_1 v + k_2 v^{1/2} \tag{3}$$

Fig. 3. Electrochemical energy storage performance of the DID-MnS/MnO and SD-MnS cathodes in a three-electrode system. (a) Comparison of CV curves at a scan rate of 0.2 mV/s, (b) 1st, 2nd, and 3rd CV curves of DID-MnS/MnO at 1.0 mV/s, (c) GCD curves at different current densities of the DID-MnS/MnO cathode, (d) Comparison of discharge specific capacity at 0.1 A/g, (e) Comparison of cycling performance and Coulombic efficiency at 1.0 A/g, (f) Rate performance comparison at different current densities, (g) Capacity comparison with other reported cathode materials in aqueous magnesium-ion batteries, and (h) Comparison of Nyquist plots at open-circuit voltage (the inset shows the equivalent circuit diagram).

or

$$i/v^{1/2} = k_1 v^{1/2} + k_2 \qquad (4)$$

where i represents the current value under the static potential (V), k_1 represents the ratio of pseudocapacitance control, and k_2 signifies the diffusion control ratio. Fig. 4c-d illustrate that the pseudocapacitance contribution percentages for DID-MnS/MnO vary from 34 %, 43 %, 45 %, 52 %, and 62 % at different scan rates ranging between 0.2 mV/s and 1.0 mV/s. Conversely, SD-MnS demonstrates values ranging from 22 %, 25 %, 27 %, 31 %, and 41 %, as shown in Fig. S11c-d (Supplementary Information). It is evident that the capacitance contribution of both materials increases with the scanning rate, and the capacitance contribution ratio of DID-MnS/MnO surpasses that of SD-MnS significantly. Thus, it can be inferred that the charge storage controlled by pseu-

docapacitance constitutes a substantial portion of the total capacity in the DID-MnS/MnO cathode, thereby imparting excellent rate performance compared to the pristine SD-MnS cathode [47]. It is worth noting that the curve fitted by the capacitance contribution calculation results exceeds the range of the original CV curve, which may be caused by two reasons. (1) Not considering the impact of overpotential caused by resistance on voltage; (2) Residual current when scanning direction reversal is not corrected [48]. Subsequently, to further verify the reaction mechanism, ex-situ XRD characterization was performed on different electrodes at different charging or discharging potentials (A-G), as shown in Fig. 4e for the selected potential distribution, and Fig. 4f for the characterization results. According to the Bragg formula [13]:

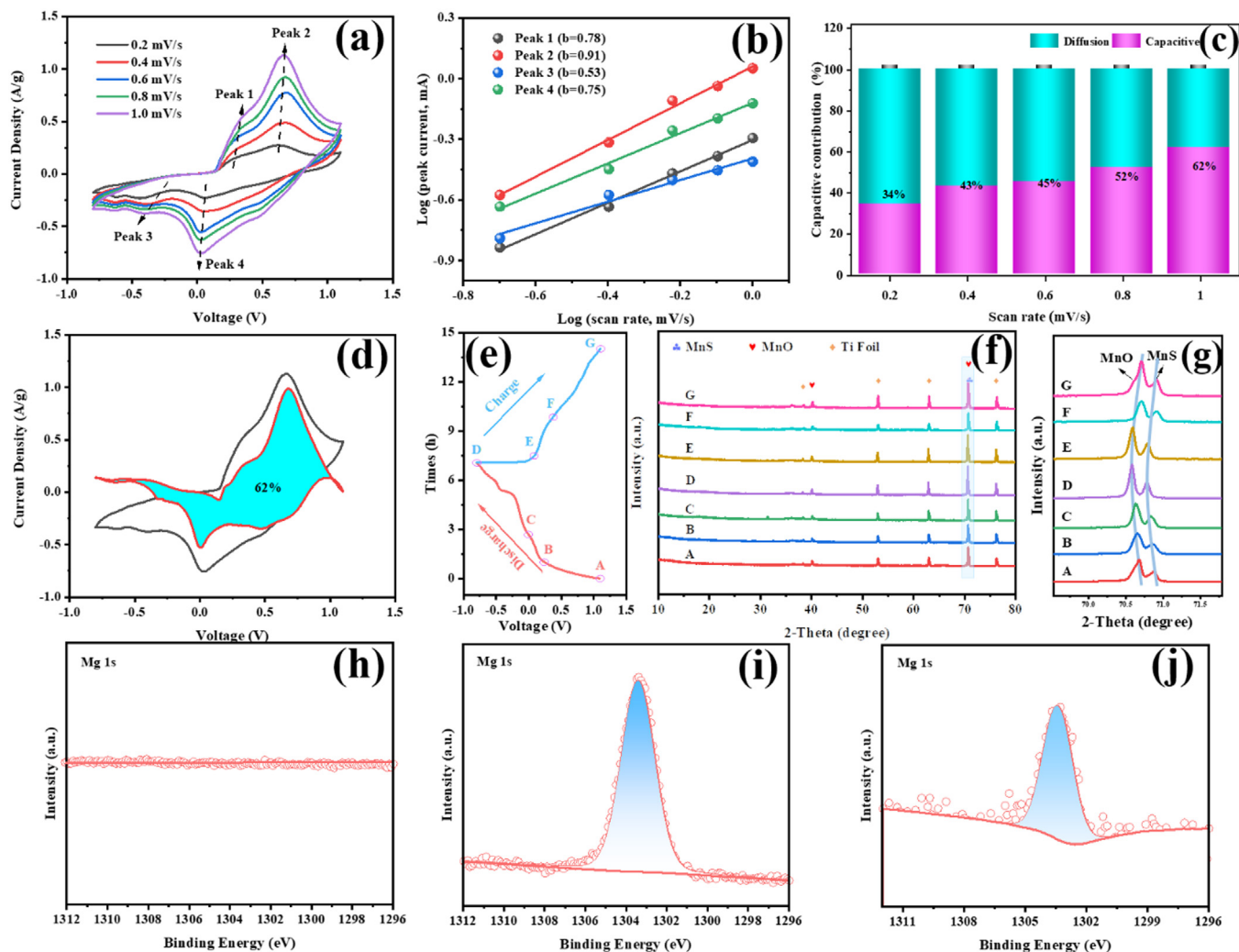$$2d\sin\theta = n\lambda \qquad (5)$$

Fig. 4. Analysis of the electrochemical kinetics and energy storage mechanism of DID-MnS/MnO. (a) CV curves of the DID-MnS/MnO electrode at scan rates of 0.2, 0.4, 0.6, 0.8 and 1.0 mV/s, (b) log(*i*) versus log(*v*) plots of the corresponding four redox peaks in the CV curves, (c) Capacitive contributions at scan rates of 0.2, 0.4, 0.6, 0.8 and 1.0 mV/s in the 0.5 M MgSO$_4$ electrolyte, (d) Proportion of capacitance contribution to the total capacity at a scan rate of 1 mV/s, (e) GCD diagram of one cycle at steady state, (f-g) Ex-situ XRD patterns at selected charge/discharge states and the partial magnified signals diagram, (h) Original, (i) fully discharged and (j) fully charged electrode for ex situ XPS patterns of Mg 1 s.

when Mg^{2+} is embedded in the host material during the discharge process, the material undergoes lattice expansion, causing the diffraction peak to shift towards a lower angle. During the charging process, when Mg^{2+} is extracted from the host material, the lattice gradually reverts to its initial state, and the diffraction peak returns to its original angle [39]. As depicted in Fig. 4g, the diffraction peak angle undergoes a notable leftward shift during the A-D process, while during the D-G process, it shifts to the right. These two diffraction peaks correspond to MnO and MnS, respectively, indicating that the primary energy storage mechanism of Mg^{2+} in the host material is insertion/deinsertion. Furthermore, the ex-situ XPS test results of Mg 1s presented in Fig. 4 h-j corroborate the aforementioned conclusion. In its original state, Mg^{2+} is absent in the material (Fig. 4h). When fully discharged, Mg was detected (Fig. 4i), and the intensity is significantly greater than that when fully charged (Fig. 4j), fur-

ther proving the insertion/deinsertion mechanism of Mg^{2+} in DID-MnS/MnO. Furthermore, Fig. S12 in the Supplementary Information illustrates the EDS image of the material in its fully charged state. It should be emphasized that, in contrast to the fully charged condition, the EDS image when the material is fully discharged (as shown in Fig. S13, Supplementary Information) reveals a notable increase in the Mg element (4.5 %→15.9 %). This observation serves as further evidence that the mechanism of energy storage in this material involves the insertion and removal of Mg^{2+} ions within the host structure.

Moreover, using the exceptional electrochemical characteristics of the DID-MnS/MnO, an aqueous magnesium ion capacitor (AMIC) was constructed. This AMIC employs either DID-MnS/MnO or SD-MnS as the cathode, activated carbon as the anode, and 0.5 M MgSO$_4$ as the electrolyte solution. The capacity ratios of the anode to cathode in DID-MnS/MnO//AC and SD-MnS//AC AMICs were found
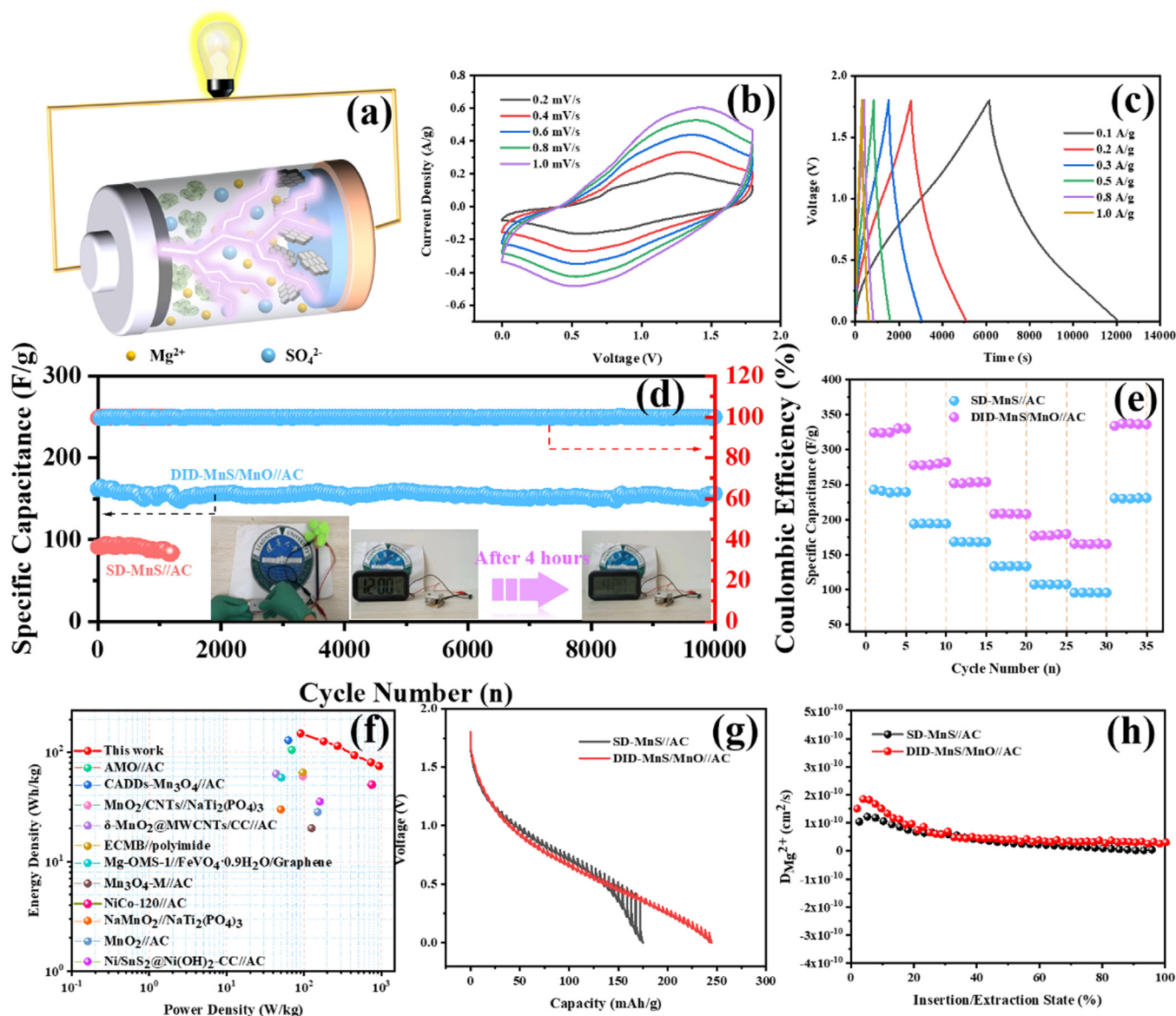
Fig. 5. The electrochemical performance of the DID-MnS/MnO//AC and SD-MnS//AC AMIC in 0.5 M MgSO$_4$. (a) The AMIC installation diagram, (b) CV curves of the DID-MnS/MnO//AC AMIC, (c) GCD curves of the DID-MnS/MnO//AC AMIC, (d) Cycle performance at 1.0 A/g and the successful application of DID-MnS/MnO//AC AMIC in blower and alarm mode, (e) Comparison of the rate performance at 0.1–1.0 A/g, (f) Ragone plots of the DID-MnS/MnO//AC AMIC, (g) GITT curves of discharge, (h) Corresponding Mg^{2+} diffusion coefficient in the discharge process.

to be 10.57 and 4.59, respectively. The assembly of the DID-MnS/MnO//AC AMIC is depicted in Fig. 5a, alongside a comparison with the assembly of the SD-MnS//AC AMIC. Fig. 5b and Fig. S14 in the Supplementary Information display the CV curves for both AMIC configurations at various scan rates ranging from 0.2 to 1.0 mV/s and operating voltages between 0 and 1.8 V [49]. The near-rectangular shape of the CV curves, indicative of capacitance, suggests enhanced electrochemical performance in the DID-MnS/MnO//AC AMIC due to the synergistic effect of Mn and S defects. GCD curves for both AMIC configurations, presented in Fig. 5c and Fig. S15, demonstrate the DID-MnS/MnO//AC AMIC's superior reversibility and long-term cycling performance, even at higher current densities. Ad-

ditionally, a comparison of GCD curves at a 1.0 A/g current density (Fig. S16) shows the DID-MnS/MnO//AC AMIC outperforming the SD-MnS//AC AMIC in discharge time and specific capacitance. The long-term cycling performance and Coulombic efficiency of both AMIC configurations are compared in Fig. 5d. The DID-MnS/MnO//AC AMIC exhibited remarkable cyclic stability and reversibility, maintaining a specific capacitance of 155.1 F/g after 10,000 cycles, with a capacity retention rate of 94.3 %. In contrast, the capacity retention rate of SD-MnS//AC AMIC was only 87.1 % after 1200 cycles. This indicates that under the combined action of Mn-defect and S-defect, the DID-MnS/MnO//AC AMIC demonstrates strong cyclic stability and reversibility. Additionally, the DID-MnS/MnO//AC AMIC has been suc-

cessfully applied to power a fan and alarm clock. Notably, the alarm clock can sustain operation for more than 4 h. Fig. S17 (Supplementary Information) provides a record of the alarm clock's status over 4 h at various time points. The comparison chart of specific capacitance in Fig. 5e illustrates that at different current densities (0.1, 0.2, 0.3, 0.5, 0.8, 1.0 A/g) within the range of 0.1–1.0 A/g, the specific capacitance of the DID-MnS/MnO//AC AMIC is significantly higher than that of the SD-MnS//AC AMIC. Specifically, the specific capacitance values are 330.2, 282.1, 253.8, 208.6, 179.5, and 165.7 F/g for DID-MnS/MnO//AC AMIC, compared to 242.9, 194.3, 168.3, 133.7, 107.6, and 95.6 F/g for SD-MnS//AC AMIC, respectively. Furthermore, its energy-power density characteristics surpass those of most reported Mg-ion devices (Fig. 5f, Table S2, Supplementary Information). Moreover, when the current density returned to 0.1 A/g, the specific capacitance retention of the DID-MnS/MnO//AC AMIC reached 100 %, further confirming the high reversibility of the double defect structure. To elucidate the differences in Mg^{2+} diffusion kinetics between the DID-MnS/MnO//AC and the SD-MnS//AC AMIC, and to showcase their impact on energy storage performance, we conducted a galvanostatic intermittent titration technique (GITT) test (Fig. 5g-h). By computation, it was determined that the Mg^{2+} diffusion coefficient ($D_{Mg^{2+}}$) of the DID-MnS/MnO//AC AMIC ranges from 2.6×10^{-11} to 1.9×10^{-10} cm^2/s, significantly higher than the value of the SD-MnS//AC AMIC (2.1×10^{-12} to 1.2×10^{-10} cm^2/s). Consequently, the DID-MnS/MnO//AC AMIC exhibits a large diffusion coefficient, facilitating rapid Mg^{2+} diffusion to deliver excellent electrochemical performance. Additionally, a comparison of the EIS of the DID-MnS/MnO//AC and the SD-MnS//AC AMIC (Fig. S18, Supplementary Information) reveals that the R_{ct} value of the DID-MnS/MnO//AC AMIC is 1.694 Ω, significantly lower than that of the SD-MnS//AC AMIC (5.317 Ω), suggesting that the DID-MnS/MnO//AC AMIC, owing to the dual defects of anions and cations, exhibits better kinetics. These corroborative analyses indicate that DID-MnS/MnO offers valuable insights for the swift advancement of energy storage system construction in the future and lays the groundwork for the development of magnesium ion energy storage devices.

3. Conclusion

In summary, the design of the DID-MnS/MnO through in-situ initiation of early electrochemical processes, and its application in AMICs, addresses the challenge posed by the large hydration radius of Mg^{2+} and its strong electrostatic interaction with principal materials; thus, advancing the development of aqueous magnesium ion energy storage devices. The DID-MnS/MnO prepared not only contains S defects but also generates Mn defects through in-situ induction during the initial electrochemical process, reducing the average valence state of Mn^{2+}. MnS and MnO were successfully transformed into cathode materials for Mg^{2+} with high electrochemical activity and exhibited remarkable electrochemical performance. It

is noteworthy that the aqueous magnesium ion energy storage device achieved a capacity retention rate of 94.7 % after 1200 cycles at a current density of 1.0 A/g. Furthermore, the produced AMIC achieved 94.3 % capacity retention after 10,000 cycles at a current density of 1.0 A/g. The energy storage mechanism of Mg^{2+} insertion/deinsertion in DID-MnS/MnO was elucidated through ex-situ XRD, ex-situ XPS, and EDS spectra. Therefore, the DID-MnS/MnO with dual ion defects envisioned in this study is anticipated to serve as a promising candidate for new cathode materials in the clean energy domain, offering insights for the advancement of other aqueous energy storage devices.

Declaration of competing interest

The authors declare that they have no known competing financial interests or personal relationships that could have appeared to influence the work reported in this paper.

CRediT authorship contribution statement

Minghui Liu: Writing – original draft, Formal analysis, Data curation, Conceptualization. **Mudi Li:** Visualization, Validation. **Siwen Zhang:** Writing – review & editing, Supervision, Resources, Funding acquisition, Conceptualization. **Yaxi Ding:** Visualization, Validation. **Ying Sun:** Data curation. **Jiazhuo Li:** Validation. **Haixi Gu:** Data curation. **Bosi Yin:** Writing – review & editing, Supervision, Resources, Formal analysis. **Hui Li:** Visualization. **Tianyi Ma:** Writing – review & editing, Supervision, Funding acquisition, Formal analysis.

Acknowledgements

Supplementary materials

Supplementary material associated with this article can be found, in the online version, at doi:10.1016/j.jma.2024.04. 036.

References

[1] X. Huang, Q.W. Dai, Q. Xiang, N. Yang, G.P. Zhang, A. Shen, W.M. Li, J. M. Alloy 12 (2024) 443–463.

[2] Y.Q. Zhou, F. Sun, G.N.H. Lin, S. Zanna, A. Seyeux, P. Marcus, J. Swiatowska, J. M. Alloy 12 (2024) 825–839.

[3] Y.P. Zhu, X.R Guo, Y.J. Lei, W.X. Wang, A.H. Emwas, Y.Y. Yuan, Y. He, H.N. Alshareef, Energy Environ. Sci. 15 (2022) 1282–1292.

[4] M.D Li, Y.X. Ding, Y. Sun, Y.J. Ren, J.Z. Yang, B.S. Yin, H. Li, S.W. Zhang, T.Y. Ma, Mater. Rep. Energy 2 (2022) 100161.

[5] C.Y. Sun, H.L. Wang, F.X. Yang, A.T. Tang, G.S. Huang, L.J. Li, Z.T. Wang, B.H. Qu, C.H. Xu, S.S. Tan, X.Y. Zhou, J.F. Wang, F.S. Pan, J. M. Alloy 11 (2023) 840–850.

[6] C.Y. Sun, G.S. Huang, C.H. Xu, L.J. Li, A.T. Tang, X.Y. Zhou, J.F. Wang, F.S. Pan, Energy Storage Mater. 66 (2024) 103197.

[7] M Deng, L.Q. Wang, B. Vaghefinazari, W. Xu, C. Feiler, S.V. Lamaka, D. Höche, M.L. Zheludkevich, D. Snihirova, Energy Storage Mater. 43 (2021) 238–247.

[8] Z. Ding, Y.T. Li, H. Yang, Y.F. Lu, J. Tan, J. Tan, J.B. Li, Q. Li, Y.A. Chen, L.L. Shaw, F.S. Pan, J. M. Alloy 10 (2022) 2946–2967.

[9] H. Yang, Z. Ding, Y.T. Li, S.Y. Li, P.K. Wu, Q.H. Hou, Y. Zheng, B. Gao, K.F. Huo, W.J. Du, L.L. Shaw, Rare Met. 42 (2023) 2906–2927.

[10] Z.X. Liu, L.P Qin, X.X. Cao, J. Zhou, A.Q. Pan, G.Z. Fang, S.Y. Wang, S.Q. Liang, Prog. Mater. Sci. 125 (2022) 100911.

[11] Y. Liu, H. Chen, X.M. Lou, X.Y. Wen, Z.G. Yin, K.X. Xiang, Ionics 29 (2023) 1479–1486.

[12] Y.X. Ding, S.W. Zhang, J.Z. Li, Y. Sun, B.S. Yin, H. Li, Y. Ma, Z.Q. Wang, H. Ge, D.W. Su, T.Y. Ma, Adv. Funct. Mater. 33 (2022) 2210519.

[13] M.D. Li, Y.X. Ding, S.W. Zhang, Y. Sun, M.H. Liu, J.W. Zhao, B.S. Yin, T.Y. Ma, Small Struct. 5 (2023) 2300371.

[14] X. Gao, B.Y. Wang, Y. Zhang, H. Liu, H.K. Liu, H. Wu, S.X. Dou, Energy Storage Mater. 16 (2019) 46–55.

[15] Y. Ma, Y.J. Ma, G.T. Kim, T. Diemant, R.J. Behm, D. Geiger, U. Kaiser, A. Varzi, S. Passerini, Adv. Energy Mater. 9 (2019) 1902077.

[16] Y.M. Sun, X.L. Hu, W. Luo, F.F. Xia, Y.H. Huang, Adv. Funct. Mater. 23 (2013) 2444–2463.

[17] X.M. Tang, G. Sui, Q. Cai, W.H. Zhong, X.P. Yang, J. Mater. Chem. A 4 (2016) 2082–2088.

[18] K.Y. Yasoda, S. Kumar, M.S. Kumar, K. Ghosh, S.K. Batabyal, Mater. Today Chem. 19 (2021) 100394.

[19] J.G. Wang, H.Y. Liu, H.Z. Liu, Z.H. Fu, D. Nan, Chem. Eng. J. 328 (2017) 591–598.

[20] S.M. Guo, G.X. Lu, S. Qiu, J.R. Liu, X.Z. Wang, C.Z. He, H.G. Wei, X.R. Yan, Z.H. Guo, Nano Energy 9 (2014) 41–49.

[21] Y.Q. Zhang, L. Tao, C. Xie, D.D. Wang, Y.Q. Zou, R. Chen, Y.Y. Wang, C.K. Jia, S.Y. Wang, Adv. Mater. 32 (2020) 1905923.

[22] T. Xiong, Z.G. Yu, H.J. Wu, Y.H. Du, Q.D. Xie, J.S. Chen, Y.W. Zhang, S.J. Pennycook, W.S.V. Lee, J.M. Xue, Adv. Energy Mater. 9 (2019) 1803815.

[23] N. Zhang, F.Y. Cheng, Y.C. Liu, Q. Zhao, K.X. Lei, C.C. Chen, X.S. Liu, J. Chen, J. Am. Chem. Soc. 39 (2019) 12894–12901.

[24] D. Shi, M.Z. Yang, B.G. Zhang, Z.Z. Ai, H.X. Hu, Y.L. Shao, J.X. Shen, Y.Z. Wu, X.P. Hao, Adv. Funct. Mater. 32 (2021) 2108843.

[25] Y.J. Wang, H. Wu, L. Huang, H. Zhao, Z.F. Liu, X.C. Chen, H. Liu, Y. Zhang, Inorg. Chem. 57 (2018) 7993–8001.

[26] F. Tang, X.S. Wu, Y.Q. Shen, Y.H. Xiang, X.M. Wu a, L.Z. Xiong, X.W. Wu, Energy Storage Mater. 52 (2022) 180–188.

[27] X.L. Yi, W. He, X.D. Zhang, G.H. Yang, Y.Y. Wang, J. Alloy Compd. 735 (2018) 1306–1313.

[28] R. Ramachandran, M. Saranya, A.N. Grace, F. Wang, RSC Adv. 7 (2017) 2249–2257.

[29] X.D. Zhang, X. He, S. Yin, W.L. Cai, Q. Wang, H. Wu, K.P. Wu, Y. Zhang, Inorg. Chem. 61 (2022) 8366–8378.

[30] S. Sambasivam, C.V.V.M. Gopi, H.M. Arbi, Y.A. Kumar, H.J. Kim, S.A. Zahmi, I.M. Obaidat, J. Energy Storage 36 (2021) 102377.

[31] K. Wang, K.J. Zhao, Y.P. Wang, H.H. Li, H.B. Jiang, L. Chen, J. Alloy Compd. 860 (2021) 158451.

[32] N. Luo, C. Chen, D.M. Yang, W.Y. Hu, F.Q. Dong, Appl. Catal. B 299 (2021) 120664.

[33] X. Wang, Y.W. Zhang, H.N. Si, Q.H. Zhang, J. Wu, L. Gao, X.F. Wei, Y. Sun, Q.L. Liao, Z. Zhang, K. Ammarah, L. Gu, Z. Kang, Y. Zhang, J. Am. Chem. Soc. 142 (2020) 4298–4308.

[34] Y.H. Ma, D.F. Leng, X.M. Zhang, J.J. Fu, C.R. Pi, Y. Zheng, B. Gao, X.G. Li, N. Li, P.K. Chu, Y.S. Luo, K.F. Huo, Small 18 (2022) 2203173.

[35] Y.J. Zhao, S.X. Zhang, Y.Y. Zhang, J.R. Liang, L.T. Ren, H.J. Fan, W. Liu, X.M. Sun, Energy Environ. Sci. 17 (2024) 1279–1290.

[36] Y.C. Zhang, S. Ullah, R.R. Zhang, L. Pan, X.W. Zhang, J.J. Zou, Appl. Catal. B 277 (2020) 119247.

[37] D. Cortecchia, H. Mro´z, S. Neutzner, T. Borzda, G. Folpini, R. Brescia, A. Petrozza, Chemistry 5 (2019) 2146–2158.

[38] K. Shim, K.D. Seo, H.J. Kim, Adv. Funct. Mater. 33 (2023) 2210549.

[39] Y.X. Ding, S.W. Zhang, M. Bat-Erdene, J.Z. Li, Y. Sun, M.D. Li, M.H. Liu, H. Li, Y.W. Zhang, H. Ge, G.Q. Zhao, Z.G. Yu, B.S. Yin, T.Y. Ma, Energy Storage Mater. 63 (2023) 103010.

[40] X.Y. Liu, J. Yi, K. Wu, Y. Jiang, Y.Y. Liu, B. Zhao, W.R. Li, J.J. Zhang, Nanotechnology 31 (2020) 122001.

[41] C.Y. Zhu, G.Z. Fang, S.Q. Liang, Z.X. Chen, Z.Q. Wang, J.Y. Ma, H. Wang, B.Y. Tang, X.S. Zheng, J. Zhou, Energy Storage Mater. 24 (2020) 394–401.

[42] B. Wen, C. Yang, J. Wu, J.H. Liu, W.K. Wang, J.H. Yang, X.W. Chi, Y. Liu, Chem. Eng. J. 435 (2022) 134997.

[43] Y.T. Chu, L.Y. Guo, B.J. Xi, Z.Y. Feng, F.F. Wu, Y. Lin, J.C. Liu, D. Sun, J.K. Feng, Y.T. Qian, S.L. Xiong, Adv. Mater. 8 (2018) 1704244.

[44] J. Li, H.Z. Wan, B. Zhang, C. Wang, Y. Gan, Q.Y. Tan, N.Z. Wang, J. Yao, Z.H. Zheng, P. Liang, J. Zhang, H.B. Wang, L. Tao, Y. Wang, D.L. Chao, H. Wang, Adv. Energy Mater. 11 (2021) 2003203.

[45] F.Z. Chen, D. Shi, M.Z. Yang, H.H. Jiang, Y.L. Shao, S.Z. Wang, B.G. Zhang, J.X. Shen, Y.Z. Wu, X.P. Hao, Adv. Funct. Mater. 31 (2020) 2007132.

[46] V. Augustyn, P. Simon, B. Dunn, Energy Environ. Sci. 7 (2014) 1597–1614.

[47] K. Wang, S.J. Li, X. Chen, J.S. Shen, H.L. Zhao, Y. Bai, ACS Nano 18 (2024) 7311–7323.

[48] X.J. Pu, D. Zhao, C.L. Fu, Z.X. Chen, S.N. Cao, C.S. Wang, Y.L. Cao, Angew. Chem. Int. Ed. 60 (2021) 21310–21318.

[49] J. Li, J.H. Zhang, L. Yu, J.Y. Gao, X.Y. He, H.H. Liu, Y.M. Guo, G.Q. Zhang, Energy Storage Mater. 42 (2021) 705–714.